Determination of Mouse Skeletal Muscle Architecture Using Three-Dimensional Diffusion Tensor Imaging

Anneriet M. Heemskerk,[1*] Gustav J. Strijkers,[1] Anna Vilanova,[2] Maarten R. Drost,[3] and Klaas Nicolay[1]

Muscle architecture is the main determinant of the mechanical behavior of skeletal muscles. This study explored the feasibility of diffusion tensor imaging (DTI) and fiber tracking to noninvasively determine the in vivo three-dimensional (3D) architecture of skeletal muscle in mouse hind leg. In six mice, the hindlimb was imaged with a diffusion-weighted (DW) 3D fast spin-echo (FSE) sequence followed by the acquisition of an exercise-induced, T_2-enhanced data set. The data showed the expected fiber organization, from which the physiological cross-sectional area (PCSA), fiber length, and pennation angle for the tibialis anterior (TA) were obtained. The values of these parameters ranged from 5.4–9.1 mm^2, 5.8–7.8 mm, and 21–24°, respectively, which is in agreement with values obtained previously with the use of invasive methods. This study shows that 3D DT acquisition and fiber tracking is feasible for the skeletal muscle of mice, and thus enables the quantitative determination of muscle architecture. Magn Reson Med 53:1333–1340, 2005. © 2005 Wiley-Liss, Inc.

Key words: muscle fiber architecture; diffusion tensor imaging; fiber tracking; exercise-induced T_2 enhancement; mice

Muscle architecture is the main determinant of the mechanical behavior of skeletal muscles (1–3). This architecture, which is defined as the arrangement of muscle fibers relative to the axis of force generation (3), is characterized by various parameters, including muscle length, fiber length, pennation angle, and physiological cross-sectional area (PCSA). The pennation angle is the angle between the muscle fibers and the tendon plate, while the PCSA is the sum of the cross-sectional areas of all fibers. The PCSA is the architectural parameter that is directly proportional to the maximum force generated by the muscle (3). However, the PCSA is also the parameter that is the most difficult to measure, and is therefore normally indirectly determined from the muscle volume and fiber length (4).

The fiber length and pennation angle can be determined by ultrasonography (US) (5) and anatomical reconstruction methods. However, both of these techniques have severe limitations. US does not account for spatial variation in fiber length and orientation within a muscle. The disadvantage of traditional anatomical reconstruction techniques is that they are restricted to ex vivo preparations (2), which precludes the use of longitudinal studies. An alternative, noninvasive method used to measure the skeletal muscle fiber structure is magnetic resonance imaging (MRI). This method may enable the reconstruction of whole muscles and provide the desired architectural parameters, including the PCSA.

MRI offers researchers an opportunity to study the microstructure of tissues such as brain white matter (6,7), heart muscle (8,9), and skeletal muscle (6,10–14) using diffusion tensor imaging (DTI). DTI relies on the fact that the self-diffusion of water in tissue is restricted by membranes and other cellular constituents, resulting in an apparent diffusion coefficient (ADC), which is lower than the free diffusion coefficient and is orientation-dependent for elongated structures. One can characterize the orientation dependency by measuring the diffusion with MRI in at least six directions, and the DT can be calculated from this measurement. The eigenvalues and eigenvectors derived from this tensor provide information on the local tissue geometry. It has been shown that for skeletal muscle the eigenvector with the largest eigenvalue (i.e., the principal eigenvector) corresponds to the long axis of the muscle fibers (11,12). These local, voxel-based directions can be combined by a fiber-tracking algorithm (15,16) to reconstruct the paths of muscle fibers in the tissue (13).

The mechanisms of force loss that occur during progressive muscular diseases caused by genetic defects (e.g., Duchenne's muscular dystrophy and Pompe's disease) are increasingly being studied in genetically modified mice (17,18). Such diseases generally cause both progressive muscle wasting and a decrease in maximal tension. This wasting also causes changes in muscle architecture. As stated above, the fiber architecture is the main determinant of mechanical behavior. Therefore, to determine any actual loss in muscle quality, one must know the architecture. The DTI-based fiber-reconstruction method is expected to facilitate the study of architectural changes in mice, which is a most challenging application because of the small size of mouse muscles.

The aim of this study was to develop the methods to determine the in vivo 3D architecture of mouse skeletal muscle, using DTI. We will show that with this approach it is possible to calculate the PCSA and determine the fiber length and the pennation angle of the tibialis anterior (TA) muscle, which can be easily identified and has been extensively studied. The methods used were an in vivo 3D acquisition, a fiber-tracking algorithm, and analysis and visualization tools. For part of this study we focused on the possibility that fibers might erroneously cross muscle borders. We indirectly delineated these borders using T_2

[1]Biomedical NMR, Department of Biomedical Engineering, Eindhoven University of Technology, Eindhoven, The Netherlands.

[2]Biomedical Image Analysis, Department of Biomedical Engineering, Eindhoven University of Technology, Eindhoven, The Netherlands.

[3]Department of Movement Sciences, Maastricht University, Maastricht, The Netherlands.

*Correspondence to: Anneriet Heemskerk, Department of Biomedical Engineering, Eindhoven University of Technology, P.O. Box 513, 5600 MB, Eindhoven, The Netherlands. E-mail: a.m.heemskerk@tue.nl

Received 12 October 2004; revised 15 December 2004; accepted 29 December 2004.

DOI 10.1002/mrm.20476

Published online in Wiley InterScience (www.interscience.wiley.com).

enhancement caused by exercise of the dorsal flexor muscles.

MATERIALS AND METHODS

Specimen

Experiments ($N = 6$) were performed on male C57BL/6 mice (26.5 ± 1.4 g, mean ± SD) that were positioned in an MRI-compatible device (19). The mice were anesthetized with isoflurane (Schering-Plough, Animal Health, Maarssen, The Netherlands), 1.0–1.5% in air, with a flow rate of 0.4 l/min, controlled by a flow meter system (UNO, Zevenaar, The Netherlands). The anesthesia was delivered to the mouse via a facemask. The mouse's left foot was cast in a plaster shoe and glued to a fixation plate with an ankle angle of 90°. A hip fixation unit secured the position of the hip (20). The animal's body temperature was maintained at 36–39°C with a warm-water blanket (38°), and its respiration was continuously monitored with an ECG/respiratory trigger unit (Rapid Biomedical, Würzburg, Germany).

The MRI experiments consisted of a DTI measurement followed by T_2-weighted MRI with electrical stimulation of the dorsal flexors (see below).

After the MR experiments were performed, the mice were killed. All of the lower hindlimb muscles were dissected and weighed on an analytical balance. For anatomical reference, an additional animal was killed and perfusion-fixed with formaldehyde. Thereafter, the limb was embedded in plastic, and 5-μm-thick slices were stained with hematoxylin and eosin. All of the experimental procedures were approved by the Institutional Animal Care and Use Committee of Maastricht University and complied with the principles of proper laboratory animal care.

Electrical Stimulation

Exercise-induced T_2 enhancement (21,22) was used to determine the muscle boundaries of the dorsal flexors in T_2-weighted MR images. A chronically implanted electrode on the common peroneal nerve was used for electrical stimulation. This electrode was implanted 2–3 weeks before measurements were taken. The construction of the electrode and the implantation procedure were previously described by Warren et al. (23). A supramaximal voltage (2–2.5 V) was used to ensure that all of the fibers were activated. The T_2 enhancement vanished within 5 min after the end of stimulation, which made repeated stimulation during measurement necessary to maintain the change in T_2 during the time required to obtain a high-resolution image. Therefore, the stimulation protocol consisted of a tetanus (100 Hz) for 1 min prior to the MR measurement, followed by single twitches (repetition every 140 ms) during the delays in the T_2-weighted MRI measurements.

MRI

The MR measurements were performed with a horizontal 9.5-cm-bore, 270 MHz MRI scanner with a Varian imaging console (Palo Alto, CA), equipped with 380 mT/m shielded gradients with 150 μs rise time to full maximum, and a 1.5-cm solenoidal RF coil. A 3D diffusion-weighted (DW) fast spin-echo (FSE) sequence with fat suppression was used. The diffusion gradients were applied along six noncolinear directions in accordance with Jones et al. (24), and one reference image was recorded without diffusion weighting. The scan parameters were as follows: field of view (FOV) = 15 × 15 × 30 mm^3, matrix size = 60 × 60 × 128 (zero-filled to 64 × 64 × 128), resulting in an isotropic resolution of 234 μm, echo time (TE) = 10 ms, echo train length = 6, number of signal averages (NSA) = 2 and repetition time (TR) = 1 s, resulting in a total scan time for the 3D DTI measurement of 2 hr 20 min. The diffusion-weighting parameters were: gradient separation time = 20 ms, gradient duration = 10 ms, and b-value = 0 or 584 s/mm^2. Fat suppression was carried out by frequency-selective excitation followed by gradient spoiling, using three Gaussian-shaped 90° pulses with a duration of 5 ms, and spoiling gradients with a duration of 4 ms and a strength of 40 mT/m.

During the exercise protocol, 2D SE images with fat suppression were obtained with the following parameters: FOV = 15 × 15 mm^2, matrix size = 128 × 128 (zero-filled to 256 × 256), slice thickness = 1 mm, TE = 20 ms, TR = 2 s, and number of slices = 15. The scan duration was 16 min.

Data Processing

We performed an initial analysis of the DW images using Mathematica (Wolfram Research). A threshold based on the non-DW images was used to mask the regions with noise only outside the leg. The pixel intensities of the 3D DTI data set were fitted to obtain the six elements of the DT (**D**). For every data set we drew three regions of interest (ROIs) in the TA, a cross section in the middle of the muscle, and two regions at 1 mm distal and proximal, respectively. In these regions the means of the following parameters were calculated: the eigenvalues (λ_1, λ_2, and λ_3), ADC = Trace(**D**)/3, and fractional anisotropy (FA), defined as:

$$FA = \frac{\sqrt{(\lambda_1 - \lambda_2)^2 + (\lambda_2 - \lambda_3)^2 + (\lambda_1 - \lambda_3)^2}}{\sqrt{2(\lambda_1^2 + \lambda_2^2 + \lambda_3^2)}} \quad [1]$$

The volume of the activated muscles in the T_2-enhanced images was determined in ImageJ (NIH, Bethesda, MD, USA). A k-means algorithm was used to cluster pixels on the basis of intensity, after which the clustered pixels were segmented and closed. The total number of segmented pixels for each slice was calculated and converted to a volume (V_{T2}). We compared this MRI-based volume with the muscle volume as determined from the muscle mass (V_m), using a muscle density of 1.05 g/cm^3 (25) to convert mass to volume.

Fiber Tracking

Fiber tracking was performed with the use of a visualization tool for DTI data (i.e., DTITool) as described by Vilanova et al. (26). The fiber paths were calculated starting from a user-defined seed point. The seed point defines the initial position to integrate the vector field defined by the

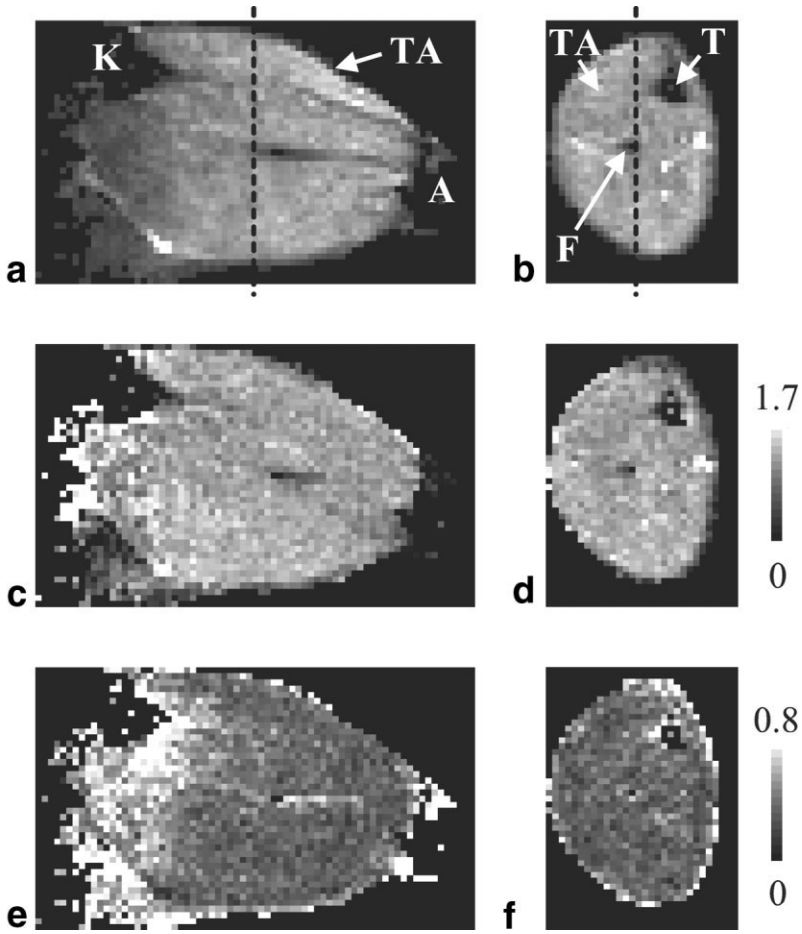

FIG. 1. Images of a mouse hindlimb obtained with a DW FSE sequence. **a:** Longitudinal slice through the lower hindlimb (relative position indicated by the dashed line in **b**). The knee (K), ankle (A), and tibialis anterior muscle (TA) are indicated. **b:** Transversal slice through the hindlimb (relative position indicated by the dashed line in **a**). The tibia (T), the fibula (F), and TA are indicated. **a** and **b:** Non-DW images. **c** and **d:** Mean ADC maps ($\times 10^{-3}$ mm^2 · s^{-1}). **e** and **f:** FA maps (-).

principal eigenvector. The integration was performed by means of a second-order Runge-Kutta scheme. An integration step of 0.2 voxel was used. Tracking was continued until the stop criteria were satisfied. A minimal FA of 0.2 and a maximal angle change of 10° per integration step were used as the stop criteria.

With the DTITool, fibers originating from different ROIs were colored differently, which enabled us to conveniently visualize the different muscle compartments. 3D stereo viewing was also possible.

Problems with the DTI method and fiber tracking were expected to occur at the boundaries between adjacent muscles, because voxels may contain signal from both muscles. Therefore, we evaluated the fiber paths at the boundaries in detail by comparing the fiber tracks with the muscle boundaries determined from T_2-enhanced images. This T_2 enhancement was employed because the muscle boundaries in these very small mouse muscles could not be determined accurately from regular high-resolution T_2-weighted images. Fibers that originated from a T_2-enhanced region were followed through the successive slices, and should remain in the enhanced regions. The high-resolution 2D T_2-enhanced images were reduced to a 64×64 matrix and assigned to the corresponding 3D slice position so that the images matched the 3D DTI data set.

The physiological parameters of the muscle were determined from the TA and the extensor digitorum longus (EDL). We determined the PCSA by selecting an ROI that included all fibers attached to the distal tendon plate. The dot product of this ROI and the corresponding principal eigenvectors resulted in the PCSA. The ROI for determining the PCSA is based on whole voxels, while in some cases only part of the fibers in some voxels can belong to the TA and EDL. The inclusion or exclusion of voxels that belong partly to the cross section introduces some variances in PCSA. We determined the range of TA fiber lengths from a group of fibers running from the distal to the proximal tendon plate. The position of the tendon plate was defined as the place at which the fibers attached from both sides and the fiber pathways continued parallel to each other. The pennation angle of the TA muscle fibers was determined from fibers running approximately through the midsagittal plane. Therefore, an ROI was defined on a cross-sectional slice with fibers attaching to the distal tendon plate. We defined the pennation angle as the maximum angle between the projection of the tendon plate and the fibers on the plane of view.

RESULTS

Figure 1a and b show two non-DW images through the hindlimb. Figure 1a shows a longitudinal slice through the limb, and Fig. 1b depicts a cross section of this leg. The 3D FSE sequence with fat suppression resulted in artifact-free images, whereas without fat suppression multiple ghosts of the fat appeared (data not shown). The knee was posi-

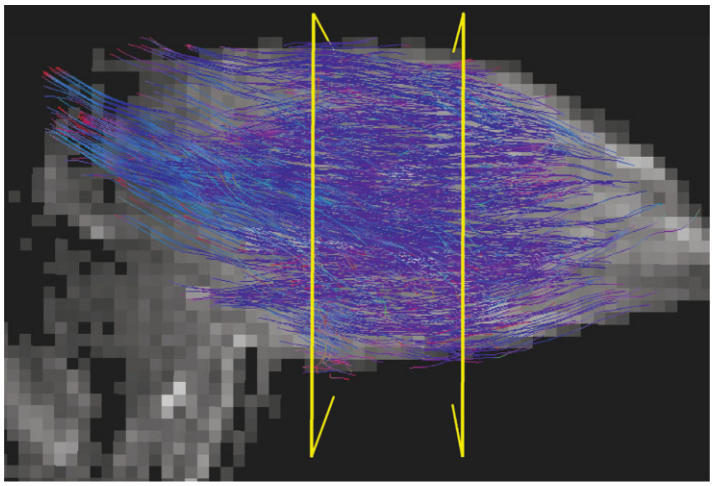

FIG. 2. Fiber tracking in the same data set as in Fig. 1. Fiber tracking was started from the two slices indicated by the yellow lines. The 3D fibers are projected on a 2D MRI slice.

tioned at the end of the coil, which explains the lower signal intensity in the proximal part of the limb. Figure 1c and d depict the corresponding mean ADC maps, which reveal a uniform diffusivity in all muscle groups. The FA maps are shown in Fig. 1e and f. The mean ADCs (±SD) for the three ROIs in this specific leg were $(1.17 \pm 0.16) \times 10^{-3}$ mm$^2 \cdot$ s^{-1}, $(1.17 \pm 0.14) \times 10^{-3}$ mm$^2 \cdot$ s^{-1}, and $(1.17 \pm 0.12) \times 10^{-3}$ mm$^2 \cdot$ s^{-1}, for the middle of the muscle and the 1-mm distal and 1-mm proximal positions, respectively. For the FA these values were 0.38 ± 0.11, 0.39 ± 0.09, and 0.37 ± 0.13, respectively. There was no significant difference in the values for the different ROIs, which applied for all the data sets.

For the TA in the six mice, the means (±SD) of the three eigenvalues λ_1, λ_2, and λ_3 were $(1.76 \pm 0.10) \times 10^{-3}$, $(1.12 \pm 0.05) \times 10^{-3}$, and $(0.77 \pm 0.05) \times 10^{-3}$ mm$^2 \cdot$ s^{-1}, respectively, while the mean ADC and FA were found to be $(1.22 \pm 0.08) \times 10^{-3}$ mm$^2 \cdot$ s^{-1}, and 0.39 ± 0.02, respectively.

Figure 2 shows an example of fiber tracks starting from the two slices indicated by the yellow lines. The fibers cover almost the whole muscle length. Visual inspection of the orientation of the fibers reveals a correspondence with known anatomy.

The stop criteria for the fiber tracking were chosen to be a minimum FA of 0.20 and a maximum angle per integration step of 10°. The minimum FA was >1 SD below the mean FA. Variation of this parameter between 0.10 and 0.30 had little effect on the result of the fiber-tracking procedure. The maximum angle per integration step had a larger influence on the tracked fibers. When a value below 10° was chosen many fibers were interrupted, while at higher values some of the fibers had a hairpin shape at positions near the tendon plates.

Exercise-induced T_2 enhancement was used to identify the boundaries of the dorsal flexor muscle complex. The T_2-weighted images (Fig. 3a) clearly showed an increased intensity in the dorsal musculature, which includes the TA, EDL, and peroneus (PE). The volume of these active muscles (V_{T2}), calculated after clustering (Fig. 3b) and segmentation (Fig. 3c) was highly correlated with the volume determined from the combined masses (V_m) of TA, EDL, and PE, with $V_{T2} = 3.64 + 1.04 V_m$ [μl] and $R^2 = 0.94$. The V_{T2} ranged from 42 to 89 μl.

The combination of fiber tracking and T_2 enhancement enabled us to critically evaluate the fiber-tracking procedure at the muscle boundaries, where fibers may erroneously jump over to nearby muscles (Fig. 4). Fibers that started from a region with activated muscles (enhanced T_2) largely remained in this muscle group, whereas other fibers that started from a region outside the activated region did not enter the enhanced region. Less than 10% of the fibers at the interface between the activated and nonactivated regions did not remain in the initial muscle.

A number of examples to illustrate the possibilities of 3D DTI and fiber tracking are depicted in Fig. 5. Figure 5a shows four ROIs containing different muscle groups, which correspond to the anatomical reference, shown on the right-hand side. The featherlike shape of the distal part of the TA is obvious in Fig. 5b. The pennation angle for

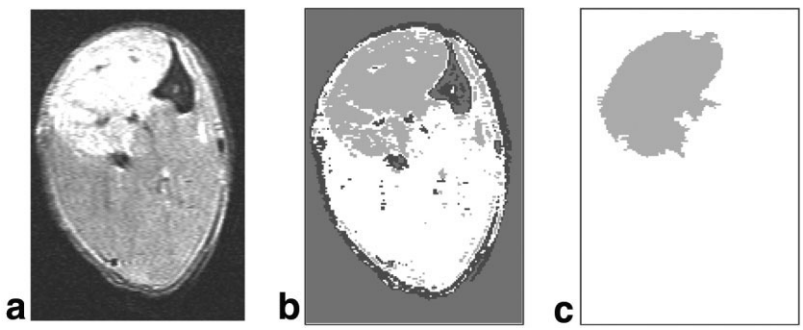

FIG. 3. Segmentation of exercise-induced, T_2-enhanced images of mouse hindlimb. **a:** T_2-weighted image with areas of increased intensity caused by stimulation of the dorsal flexor muscle complex. **b:** k-Means clustering of Fig. 3a with four cluster groups, as depicted in white, light gray, dark gray, and black. **c:** Segmentation of the activated muscle complex.

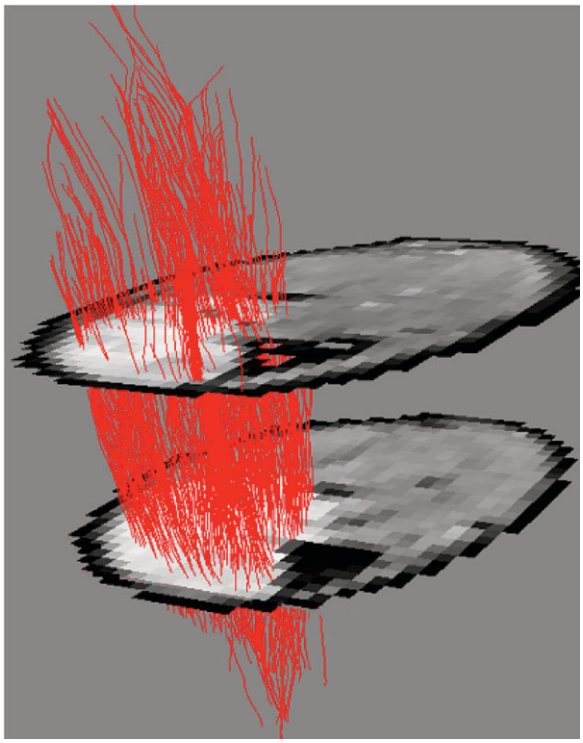

FIG. 4. Evaluation of the fiber-tracking procedure at muscle boundaries. The increased intensity of the dorsal flexor muscle complex, as shown in Fig. 3, was used to identify the muscle boundaries. Fiber tracking started from the enhanced region in the lower slice. Almost all fibers starting in the lower slice can also be identified in the upper slice, located 2 mm proximal. There is less fiber density in the upper slice than in the lower slice because of the pennation structure of the muscle, and because some fibers do not cover the whole muscle.

this example was 21°. In Fig. 5c the two tendon sheets are indicated, and the estimated fiber length for this case was 6.6 ± 0.7 mm. A reconstruction of the TA and EDL is shown in Fig. 5d, from which the PCSA was estimated to be 6.1 ± 0.7 mm^2. The PCSA, the calculated fiber length from mass and PCSA, the DTI-based fiber length, and the pennation angle for all of the mice are shown in Table 1. We were not able to determine the fiber length for every data set because it was sometimes difficult to ascertain the position of the proximal tendon sheet.

DISCUSSION

The FSE method described here was used to obtain DT images of the mouse lower hindlimb with an isotropic 3D resolution of 234 μm in 2.5 hr. DTI-based fiber tracking enabled the reconstruction of whole muscles even in areas where fibers may erroneously jump over to a nearby muscle. The muscle architectural parameters (i.e., PCSA, fiber length, and pennation angle) were successfully calculated from the data sets. The method described here offers a means of directly determining the PCSA, which is not possible with other techniques. An additional advantage is that DTI is noninvasive and thus enables the use of longitudinal studies. Therefore, this method is promising for the study of dynamic changes in muscle architecture caused by alterations in muscle activity or muscle disease.

To obtain an isotropic resolution, volume acquisition is necessary, which leads to long scan times. However, to obtain a similar resolution for a regular DW multislice SE sequence, one would need a very strong slice-selection gradient, which would lead to additional, unwanted dif-

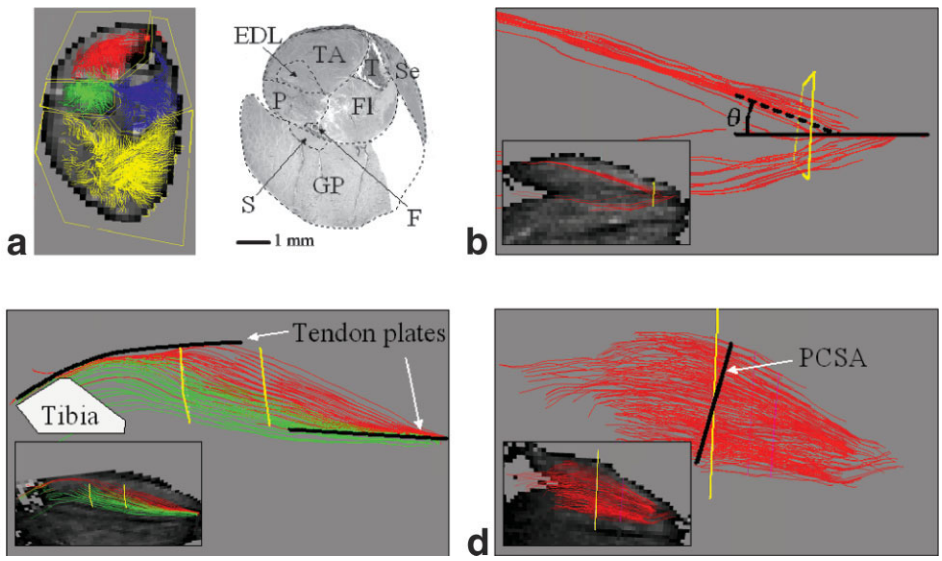

FIG. 5. Representative examples of fiber tracking in the mouse hindlimb, illustrating the architectural muscle parameters pennation angle, fiber length, and PCSA. Fiber tracking was started from the ROIs indicated with the yellow lines. Fibers originating from different ROIs are in different colors. The insets in **b–d** show the fibers projected on a 2D slice of the non-DW MR image for anatomical reference. **a:** Transversal slice showing different muscle groups that can be identified in different colors. The image on the right shows an anatomical reference from a different animal. Part of the gastrocnemius is missing due to the cutting procedure used. The structures identified with a microscope were the tibialis anterior (TA), extensor digitorum longus (EDL), peroneus (P), gastrocnemius and plantaris (GP), soleus (S), flexor (FL) and semimembranosus (Se) muscles, tibia (T), and fibula (F). **b:** The determination of the pennation angle (θ), defined as the angle between the tendon sheet (solid line) and the muscle fibers (dashed line) in the midsagittal plane of the muscle. **c:** Tracking of fibers in the TA muscle, from which the fiber length between the two tendon plates was determined. **d:** Longitudinal view of the reconstruction of fibers starting from the transversal ROI indicated with the yellow line. The black solid line represents the PCSA, defined as the dot product of the transversal ROI with the local fiber direction.

Table 1
Muscle Architectural Parameters Obtained by Fiber Tracking (Mean ± SD)*

Mouse	PCSA (mm^2)	FL_{PCSA} (mm)	FL_{DTI} (mm)	θ (deg.)
1	5.4 ± 0.3	5.2 ± 0.3	–	21 ± 1
2	7.5 ± 0.4	7.1 ± 0.4	7.8 ± 0.6	21 ± 1
3	9.1 ± 0.4	5.0 ± 0.2	6.6 ± 0.7	21 ± 2
4	8.1 ± 0.5	7.9 ± 0.4	–	22 ± 2
5	6.2 ± 0.4	6.2 ± 0.4	6.8 ± 0.5	24 ± 2
6	6.0 ± 0.3	6.3 ± 0.3	5.8 ± 0.6	24 ± 3

*The DTI-based fiber length for mouse 1 and 4 could not be determined because the position of proximal tendon plate could not be identified.
PCSA, physiological cross sectional area; FL_{PCSA}, fiber length calculated from the PCSA and the combined masses of TA and EDL; FL_{DTI}, fiber length determined from the length of the tracked fibers; θ, pennation angle.

fusion weighting. To reduce scan time, we used an FSE sequence. Although both the FSE sequence and diffusion measurements are prone to movement-related artifacts, no such artifacts were visible in the data. This led us to conclude that the present method of limb immobilization was sufficient to prevent motion artifacts. At the edges of the coil the signal intensities were lower (Fig. 1a, left side), which resulted in a larger variation of the ADC and an apparently higher FA in these regions. The diffusivities and FA index reported here are similar to values previously determined in living rats (13,27). Compared to human TA (28), the diffusivities are about 20% lower, probably due to the smaller size of the mouse muscle fibers. The FA is the same.

Tseng et al. (29) concluded that there is a geometric relation between the eigenvectors of the DT and the fiber architecture of bovine heart. They demonstrated that the three eigenvalues λ1, λ2, and λ3 correspond to the direction along the long axis of the fibers, parallel to the myocardial sheets and normal to the sheets, respectively. This finding inspired Galbán et al. (28) to propose that for skeletal muscle λ1, λ2, and λ3 represent the diffusive transport along the long axis of a muscle fiber within the endomysium and the cross-section of a muscle fiber, respectively. According to this assignment, λ3 would be dependent on the muscle fiber radius. The study by Galbán et al. (28) showed that DTI is able to distinguish functionally different human muscles on the basis of their diffusion properties, especially on the basis of differences in λ3. We did not observe a significant difference in diffusivities between the TA and the gastrocnemius. A possible explanation is that because of the combination of the lower diffusivities and small ROIs, the SD of the mean λ3 was too large to resolve possible differences in diffusion characteristics between the TA and gastrocnemius.

We were able to perform fiber tracking in the whole leg, and the fiber orientation corresponded with known fiber architecture. Fibers that started in one slice tended to converge on the tendon sheets. This is to be expected from the known fiber organization of the TA muscle, which has a featherlike shape (i.e., unipennate on the proximal tendon plate, and bipennate on the distal, internal, tendon plate). We were also able to track fiber paths within one muscle. However, near boundaries (e.g., just under the skin), the tracking appeared to be less accurate. This is probably due to partial volume effects and possibly also by some gradient-induced shift of the DW images, which resulted in a high FA at the surface (Fig. 1f). This shift was determined to be less than 1 voxel, and therefore no correction was applied. This is also why the semimembranosus is not visible in the MR image in Fig. 5a. Also near the edges of the coil, fiber tracking was less accurate due to the larger variation in the ADC. This made it more difficult to visualize the proximal tendon plate.

Although the muscle reconstruction qualitatively corresponded with known architecture, tracking of single fibers sometimes resulted in erroneous paths. The fiber tracking was sensitive to the maximum angle per integration step. Below 10° many fibers were interrupted, and above this value some of the fibers had a hairpin shape at positions near the tendon sheets. The maximum angle stopping criterion prevented folding back and sharp curvatures; however, this will not constrain the tracking of realistic muscle fiber paths since the criterion of 10° per step still allows for 200°/mm, which is well above the maximum that can be expected for muscle fiber curvature. In some mice the reconstructed pathways included both muscle fibers and the tendon plate. Fibers attached to this plate from both sides, and due to partial volume effects this can result in a net anisotropy in the direction of the tendon plate. Although this is undesirable for the reconstruction of fiber paths, it enables the detection of the tendon sheets.

Evaluation of DT-MRI-based trajectography is an important but difficult issue that also involves evaluation of the DT and the fiber paths. Extensive qualitative (14,30) and quantitative (8,31) evaluations of the DT have been performed. These evaluations were conducted to establish whether the eigenvector associated with the principal eigenvalue corresponds to the main tissue fiber direction. However, studies concerning validation of the fiber pathways are scarce. Some qualitative studies regarding the trajectography of axonal projections in the rat brain have been performed in which the positions of reconstructed fiber paths were shown to be in agreement with the locations of known neuronal pathways (16,32). Furthermore, only one study (13) reported on the validation of skeletal muscle fiber pathways. In that study it was found that the pennation angle of a group of DTI-based fibers in rat skeletal muscle correlated with the angle determined by direct anatomical inspection.

To date, no studies have described fiber tracking in distinct but nearby muscles. In such situations, fibers within one muscle may appear to enter a fiber bundle in another muscle, resulting in anatomically wrong tracks. In this study, we attempted to investigate this problem by following the fiber paths near muscle boundaries. Toward that end, we determined the boundary between the dorsal flexors and the rest of the muscles by exercise-induced T_2 enhancement. To validate these boundaries, we compared the muscle volume with the muscle mass determined by weighing. The correlation between these two parameters was high. Differences resulted from at least three possible causes: First, the mass determination also included a part of the tendon-sheet, resulting in an overestimation of the V_m. Second, the peripheral parts of the muscle were hard to visualize in the T_2-weighted scan, which caused an underestimation of V_{T2}. Third, stimulation caused a slight

expansion of the muscle, on the order of 5–10% (33). Nevertheless, the correlation between V_{T2} and V_m was high, and none of these three variations influenced the division between the active and nonactive muscles. In conclusion, exercise-induced T_2-enhanced images can be used to identify muscle boundaries.

These muscle boundaries were used in this study to investigate whether fibers erroneously jump over into a nearby muscle. This was the case for less than 1% of the total fibers in the dorsal muscle complex. It was found that less than 10% of the fibers in the interface region crossed the border between activated and nonactivated regions. Those fibers that did cross the border had already started at the interface between two muscles. These fibers may be misregistered, because the size of the voxels is still larger than the boundary between the two muscles. Based on these considerations, we concluded that the number of fibers in a muscle that accidentally jumped over was acceptable, and that individual muscles can be reconstructed separately to assess their architectural parameters. Therefore, we have demonstrated the ability of DTI-based fiber tracking to discriminate between adjacent muscles, which makes additional T_2 identification in the future unnecessary.

With the methods described here, it is possible to noninvasively quantify the muscle architectural parameters without having a priori anatomical information. Several muscle groups can be separated, and the positions of the tendon plates are visible. Aside from the ability to determine the fiber length and pennation angle, which is possible with other techniques (1,2), these methods also enable determination of the PCSA. Heretofore, this important biomechanical parameter could only be determined indirectly from the muscle volume and fiber length.

The variations in the PCSA between the different mice were to a great extent caused by the large variations in muscle mass. For the data sets that revealed both tendon plates, care was taken to not include pathways that ran either into the tendon sheet or did not connect to both plates. The smaller values for the calculated fiber lengths compared to the DTI-based fiber lengths were probably caused by the inclusion of EDL muscle fibers. The DTI-based fiber length includes only TA fibers, whereas the calculated length is an average of the TA and EDL fiber lengths. It should be noted that EDL muscle fibers are shorter than TA muscle fibers (1).

In previous studies, the PCSA, optimal fiber length, and pennation angle for mouse TA obtained by dissection (1,2,34) were 5.3 $\pm$ 0.6 mm^2, 7.9 $\pm$ 0.6 mm, and 11.7 $\pm$ 1.5°, respectively, and the PCSA and fiber length for the EDL were 1.8 $\pm$ 1.6 mm^2 and 6.2 $\pm$ 2.2 mm, respectively. The main reason for the differences between these values and those reported here is that we measured at a less than optimal fiber length. Therefore, we measured a larger pennation angle and PCSA, and a smaller fiber length. Maganaris and Baltzopoulos (35) showed for human TA that a difference of 45° in the ankle angle resulted in differences of 29% and 33% in the pennation angle and fiber length, respectively. Additional differences can result from biological variances related to mouse strain and age.

The application of DTI-based fiber tracking is also suitable for human muscles, and the first results were recently reported (36). Galban et al. (36) measured changes in the pennation angle and fiber length due to contraction, and the changes were comparable to literature values. The advantage for application in humans is that a 2D EPI sequence can be used for rapid acquisition. However, care must be taken to reduce motion-related artifacts and to cover the whole muscle for architectural reconstruction while still maintaining sufficient resolution.

CONCLUSIONS

In summary, it is possible to perform 3D DTI acquisition and fiber tracking in mouse skeletal muscle. We have shown that with this method the overall muscle structure, fiber length, pennation angle, and PCSA of mouse skeletal muscle can be determined. These methods enable longitudinal studies of muscle architecture to be performed in wild-type and transgenic mice.

ACKNOWLEDGMENTS

We acknowledge Jo Habets and Gerrit van Kranenburg for their assistance with the animal experiments, and Larry de Graaf for providing technical support.

REFERENCES

1. Burkholder TJ, Fingado B, Baron S, Lieber RL. Relationship between muscle fiber types and sizes and muscle architectural properties in the mouse hindlimb. J Morphol 1994;221:177–190.
2. Lieber RL. Muscle fiber length and moment arm coordination during dorsi- and plantarflexion in the mouse hindlimb. Acta Anat (Basel) 1997;159:84–89.
3. Lieber RL, Friden J. Functional and clinical significance of skeletal muscle architecture. Muscle Nerve 2000;23:1647–1666.
4. Sacks RD, Roy RR. Architecture of the hind limb muscles of cats: functional significance. J Morphol 1982;173:185–195.
5. Rutherford OM, Jones DA. Measurement of fibre pennation using ultrasound in the human quadriceps in vivo. Eur J Appl Physiol Occup Physiol 1992;65:433–437.
6. Basser PJ, Mattiello J, LeBihan D. MR diffusion tensor spectroscopy and imaging. Biophys J 1994;66:259–267.
7. Ito R, Mori S, Melhem ER. Diffusion tensor brain imaging and tractography. Neuroimaging Clin N Am 2002;12:1–19.
8. Hsu EW, Muzikant AL, Matulevicius SA, Penland RC, Henriquez CS. Magnetic resonance myocardial fiber-orientation mapping with direct histological correlation. Am J Physiol 1998;274:H1627–H1634.
9. Geerts L, Bovendeerd P, Nicolay K, Arts T. Characterization of the normal cardiac myofiber field in goat measured with MR-diffusion tensor imaging. Am J Physiol Heart Circ Physiol 2002;283:H139–H145.
10. Napadow VJ, Chen Q, Mai V, So PT, Gilbert RJ. Quantitative analysis of three-dimensional-resolved fiber architecture in heterogeneous skeletal muscle tissue using nmr and optical imaging methods. Biophys J 2001; 80:2968–2975.
11. van Donkelaar CC, Kretzers LJ, Bovendeerd PH, Lataster LM, Nicolay K, Janssen JD, Drost MR. Diffusion tensor imaging in biomechanical studies of skeletal muscle function. J Anat 1999;194(Pt 1):79–88.
12. van Doorn A, Bovendeerd PH, Nicolay K, Drost MR, Janssen JD. Determination of muscle fibre orientation using diffusion-weighted MRI. Eur J Morphol 1996;34:5–10.
13. Damon BM, Ding Z, Anderson AW, Freyer AS, Gore JC. Validation of diffusion tensor MRI-based muscle fiber tracking. Magn Reson Med 2002;48:97–104.
14. Cleveland GG, Chang DC, Hazlewood CF, Rorschach HE. Nuclear magnetic resonance measurement of skeletal muscle: anisotrophy of the diffusion coefficient of the intracellular water. Biophys J 1976;16:1043–153.
15. Mori S, van Zijl PC. Fiber tracking: principles and strategies—a technical review. NMR Biomed 2002;15:468–480.

16. Mori S, Crain BJ, Chacko VP, van Zijl PC. Three-dimensional tracking of axonal projections in the brain by magnetic resonance imaging. Ann Neurol 1999;45:265–269.
17. Hesselink RP, Gorselink M, Schaart G, Wagenmakers AJ, Kamphoven J, Reuser AJ, van der Vusse GJ, Drost MR. Impaired performance of skeletal muscle in alpha-glucosidase knockout mice. Muscle Nerve 2002;25:873–883.
18. Watchko JF, O'Day TL, Hoffman EP. Functional characteristics of dystrophic skeletal muscle: insights from animal models. J Appl Physiol 2002;93:407–417.
19. Drost MR, Heemskerk AM, Strijkers GJ, Dekkers EC, van Kranenburg G, Nicolay K. An MR-compatible device for the in situ assessment of isometric contractile performance of mouse hind-limb ankle flexors. Pflugers Arch 2003;447:371–375.
20. Gorselink M, Drost MR, de Louw J, Willems PJ, Rosielle N, Janssen JD, van der Vusse GJ. Accurate assessment of in situ isometric contractile properties of hindlimb plantar and dorsal flexor muscle complex of intact mice. Pflugers Arch 2000;439:665–670.
21. Bratton CB, Hopkins AL, Weinberg JW. Nuclear magnetic resonance studies of living muscle. Science 1965;147:738–739.
22. Fisher MJ, Meyer RA, Adams GR, Foley JM, Potchen EJ. Direct relationship between proton T2 and exercise intensity in skeletal muscle MR images. Invest Radiol 1990;25:480–485.
23. Warren GL, Ingalls CP, Armstrong RB. A stimulating nerve cuff for chronic in vivo measurements of torque produced about the ankle in the mouse. J Appl Physiol 1998;84:2171–2176.
24. Jones DK, Horsfield MA, Simmons A. Optimal strategies for measuring diffusion in anisotropic systems by magnetic resonance imaging. Magn Reson Med 1999;42:515–525.
25. Mendez J. Density and composition of mammalian muscle. Metabolism 1960;9:184–188.
26. Vilanova A, Berenschot G., van Pul C. DTI visualization with streamsurfaces and evenly-spaced volume seeding. In: Proceedings of the VisSym Joint Eurographics/IEEE TCVG Symposium on Visualization, Konstanz, Germany, 2004. p 173–182.
27. Strijkers GJ, Drost MR, Heemskerk A.M., Kruiskamp MR, Nicolay K. Diffusion MRI and MRS of skeletal muscle. Israel J Chem 2003;43:71–80.
28. Galban CJ, Maderwald S, Uffmann K, De Greiff A, Ladd ME. Diffusive sensitivity to muscle architecture: a magnetic resonance diffusion tensor imaging study of the human calf. Eur J Appl Physiol 2004;93:253–262.
29. Tseng WY, Wedeen VJ, Reese TG, Smith RN, Halpern EF. Diffusion tensor MRI of myocardial fibers and sheets: correspondence with visible cut-face texture. J Magn Reson Imaging 2003;17:31–42.
30. Basser PJ, Mattiello J, LeBihan D. Estimation of the effective self-diffusion tensor from the NMR spin echo. J Magn Reson B 1994;103:247–254.
31. Scollan DF, Holmes A, Winslow R, Forder J. Histological validation of myocardial microstructure obtained from diffusion tensor magnetic resonance imaging. Am J Physiol 1998;275:H2308–H2318.
32. Xue R, van Zijl PC, Crain BJ, Solaiyappan M, Mori S. In vivo three-dimensional reconstruction of rat brain axonal projections by diffusion tensor imaging. Magn Reson Med 1999;42:1123–1127.
33. Ploutz-Snyder LL, Convertino VA, Dudley GA. Resistance exercise-induced fluid shifts: change in active muscle size and plasma volume. Am J Physiol 1995;269:R536–R543.
34. Shah SB, Davis J, Weisleder N, Kostavassili I, McCulloch AD, Ralston E, Capetanaki Y, Lieber RL. Structural and functional roles of desmin in mouse skeletal muscle during passive deformation. Biophys J 2004;86:2993–3008.
35. Maganaris CN, Baltzopoulos V. Predictability of in vivo changes in pennation angle of human tibialis anterior muscle from rest to maximum isometric dorsiflexion. Eur J Appl Physiol Occup Physiol 1999;79:294–297.
36. Galban CJ, Maderwald S, De Greiff A, Uffmann K, Ladd ME. Calculation of muscle fiber orientation and length in human soleus by diffusion tensor imaging. In: Proceedings of the 12th Annual Meeting of ISMRM, Kyoto, Japan, 2004. p 775.